Impact of temperature on short-range charge ordering in $LiFePO_4/FePO_4$

Souzan Hammadi,[1] Jolla Kullgren,[1] Matthew J. Wolf,[2] Daniel Brandell,[1] and Peter Broqvist[1]
[1]*Department of Chemistry, Ångström Laboratory, Uppsala University, 75121 Uppsala, Sweden*
[2]*Institute of Physical Chemistry, RWTH Aachen University, 52074 Aachen, Germany*

(Received 16 January 2024; revised 6 March 2024; accepted 12 March 2024; published 5 April 2024)

Energy is stored in a $LiFePO_4$ battery electrode through the intercalation of Li. As Li incorporate into the crystal lattice of Fe(III)PO_4, electrons reduce Fe(III) into Fe(II). The interactions of Li and its vacant site (Va) with these localized electrons (holes), so-called polarons, cause phase separation during battery operation. These fundamental interactions are however difficult to quantify using standard electronic structure calculations. In this paper, we utilize DFT+U with occupation matrix control to compute interaction energies at varying Li-Fe(II) and Va-Fe(III) pair separations. The increased energy with separation warrants the use of an electrostatic description. The DFT+U data are fitted to a Coulombic potential with two-body corrections and used in a Monte Carlo scheme. The coordination of the species determines their short-range ordering, showing that the Li and Va create chains bridged by their associated polarons which dissociate into dimers at higher temperatures. This dissociation happens at higher temperatures for Va than for Li, indicating a more pronounced clustering behavior during the formation of $FePO_4$. Notably, a significant amount of uncoordinated Li exists at elevated temperatures, challenging the simplified picture of complete Li-Fe(II) pairing.

DOI: 10.1103/PhysRevB.109.144103

I. INTRODUCTION

$LiFePO_4$ (LFP) is commonly used as an electrode material for energy storage, showing good performance and safety metrics [1]. It is characterized by its distinct phase-separation behavior [2–6]. At low temperature, this material decomposes into phases rich and poor in Li, LFP, and $FePO_4$ (FP), respectively. Intercalation of Li into the electrode causes an interplay between these phases that is not only affected by thermodynamic and kinetic properties, but also by size and strain effects as well as battery cycling conditions [7–9]. This has intrigued the scientific community since 1997, when the LFP/FP system was first introduced by Padhi *et al.* [10]. While the two-phase miscibility has been considerably investigated, it was only in 2005 that the existence of a high-temperature solid solution was identified by Delacourt *et al.* [2,11].

As Li incorporates into the $Li_{1-x}FePO_4$ crystal, so does an electron that reduces Fe(III) into Fe(II). Similarly, the removal of Li introduces vacancies (Va) and oxidation of Fe(II) into Fe(III). The change in oxidation states accompanied with lattice distortions localizes the electrons (holes) on specific iron sites, creating so-called small polarons [6]. The solid solution phase emerges by consideration of all these (Li, Va, and polarons) degrees of freedom as supported by experimental and theoretical studies [12–14]. Experiments conducted by Ellis *et al.* have shown that electrons exhibit mobility upon entering the solid solution phase, indicating a Li-Fe(II) coupling within the system [12]. This corresponds well with the calculated high binding energies of Li-Fe(II) and Va-Fe(III) in Refs. [15–17]. Together, these studies suggest that the Li-polaron mobility is strongly correlated in the solid solution.

Additionally, the LFP-FP phase diagram has only been reconstructed by explicitly considering both Li and electronic degrees of freedom [13,18]. The computationally derived phase boundaries by Zhou *et al.* using a two-lattice model and short-range multibody interactions are in qualitative agreement with experiments, showcasing both the miscibility gap and the high-temperature solid solution region [13,14]. It has been suggested that the solid solution phase obtained is not entirely random but exhibits short-range ordering [19,20]. These results show a gap in our understanding of the ordering of Li-Fe(II)/Va-Fe(III) arrangements.

The two pairs, Li-Fe(II) and Va-Fe(III), interact differently as evidenced by their respective binding energies. References [16,21] report a barrier for separating the Li/Va and its respective polaron but disagree on which of the Li-Fe(II)/Va-Fe(III) pairs interacts more strongly. The observed increase in energy associated with Li/Va and Fe(II)/Fe(III) separation, as presented in Ref. [21], demonstrates the presence of long-range electrostatic interactions. Accounting for such long-range forces has been stressed as neglecting them could lead to the occurrence of unphysical charge ordering [22].

The pronounced electrostatic interactions underpin the prevailing hypothesis that the two species remain coupled, although this assumption warrants further scrutiny. Recent findings in Ref. [23] describe the decoupling of the Li-Fe(II) pairs as a rare occurrence emphasizing their electrostatic nature while overlooking thermal effects. However, this

contrasts experimental work by Cabana *et al.* where the decoupling increases with higher temperature [24].

In this paper, we investigate the impact of temperature on the short-range ordering of Li-Fe(II) and Va-Fe(III) pairs using a multiscale modeling approach. The multiscale model has its origin in electronic structure calculations, used to quantify the fundamental interactions between Li/Va and Fe(II)/Fe(III) in $Li_xVa_{1-x}Fe(II)_xFe(III)_{1-x}PO_4$. In general, to accurately describe localized electronic states in transition metals such as iron in $LiFePO_4$, methods beyond conventional (semilocal) density functional theory (DFT) are needed [16,25,26]. Furthermore, generating a diverse data set for a correlated system of two sublattices, where one contains polarons, poses additional problems. Distortions in the cell, as well as symmetry operations, would strongly favor localization of the polarons close to the Li or Va, thereby effectively preventing sampling of larger charge separations. To overcome both these problems and enable the assessment of various possible electron configurations, DFT+U is used in conjunction with occupation matrix control (OMC), which enables site specificity without any explicit structural modification [26].

To assess the temperature dependence on the short-range charge ordering in $LiFePO_4/FePO_4$, the generated DFT+U data set is used to fit interaction models for statistical sampling with Monte Carlo (MC) simulations. One model is generated for low Li concentrations in which Li-Fe(II) pairs represent the LFP phase formation and one model at high concentration which represents the opposite case with Va-Fe(III) pairs for the FP phase. In this way, we can efficiently account for the different electrostatic conditions in LFP and FP, and independently investigate the [Li,Va] and [Fe(II), Fe(III)] sublattices and their equilibrium structures at varying temperatures.

The outline of the paper as follows. In Sec. II, the constituents of the used multiscale approach are described. Section III goes through the results starting with a presentation of the materials FP and LFP (Sec. III A) followed by a detailed investigation of the electronic properties of Fe(II) in different environments (Sec. III B). Thereafter, we go through the data set generation and analysis of the DFT+U data (Sec. III C) followed by a detailed analysis of the MC simulation results (Sec. III D). Section IV concludes the paper.

II. METHODOLOGY

To investigate the temperature-dependent properties of Li/Va-Fe(II)/Fe(III) pairs in $Li_xVa_{1-x}Fe(II)_xFe(III)_{1-x}PO_4$ at the dilute limits, efficient methods of sampling different lattice configurations are necessary. In this paper, the chosen method is lattice-based Monte Carlo sampling in which rapid energy evaluations are enabled through the use of a point-charge model with short-range two-body correction terms accounting for overlapping relaxation spheres and Pauli repulsion. This model describes the interactions between the species of interest, which for the dilute case at low Li concentrations are Li and Fe(II). Similarly, at high Li concentrations, Va are introduced at the corresponding Li sites giving Va/Fe(III) pairs. The interaction model is parametrized using data from DFT+U calculations with OMC. In the following, we describe the technical details of these methods.

A. Electronic structure calculations

Electronic structure calculations using spin-polarized DFT in the implementation with a plane-wave basis set and pseudopotentials have been performed using VASP [27,28]. The exchange-correlation energy was described by the Perdew-Burke-Ernzerhof density functional [29]. Projector augmented wave (PAW) pseudopotentials were used in all calculations [30]. Li was described by three valence electrons ($1s^2 2s^1$), oxygen by six valence electrons ($2s^2 2p^4$), phosphorous by five valence electrons ($3s^2 2p^3$), and iron by eight valence electrons ($3d^6 4s^2$). Nonspherical contributions from the gradient corrections inside the PAW spheres were included in all calculations [31]. Structural optimizations of the unit cell and atomic positions for all bulk systems were performed using the conjugate gradient algorithm, where the relaxation continued until all components of the stress tensor were less than 0.01 kbar and the forces on each atom were less than 0.01 eV/Å. The Brillouin zone was sampled using a k spacing of 0.5 $Å^{-1}$. In all calculations, the plane-wave energy cutoff was set to 600 eV.

To treat the highly correlated Fe 3d electrons, we used the rotationally invariant Hubbard correction of Dudarev *et al.* [32] with a U-J value of 4.0 eV. The choice of using 4.0 eV for the description for the Fe(II)/Fe(III) redox couple is based on work by Jain *et al.* [33]. Regardless of correcting for electron-electron repulsion as done with the Hubbard correction, special care has to be taken to ensure the correct orbital occupation. To explicitly set the electronic configuration, we have used the OMC method implemented by Allen and Watson [26]. A two-step procedure is utilized, the first step being a restrained ionic relaxation of a frozen cell with OMC and the second being a regular DFT+U calculation with full geometric relaxation (both ions and lattice) restarted using the optimized structure and wave functions from the first step. The atomic magnetic moments are initialized for all calculations. OMC has previously been used to investigate similar systems, for example polaron-assisted migration in $Li_4Ti_5O_{12}$ [34] and Jahn-Teller distortions in layered transition metal oxides [35].

B. Interaction model

A Monte Carlo approach was used to investigate the temperature dependence in Li-Fe(II) and Va-Fe(III) arrangements. To simplify, we will focus on the former case in this description. The method follows a similar procedure to the one outlined in Ref. [36], studying the interaction and clustering of charged impurities and their associated cations. In this case, the interaction model describes Li and Fe(II) in a structure consisting of two sublattices where Li ions reside on one lattice and Fe(II) on the other. The total energy is described by Eq. (1), where a_i and a_j represent the different atoms in the system:

$$E = \sum_{\langle i,j \rangle} \left[C^{r_{ij}}_{a_i a_j} + \frac{q_i q_j}{r_{ij}} \right] + \text{const.} \tag{1}$$

Short-range interactions (up to 4.2 Å) are described using pairwise terms with individual constants, $C^{r_{ij}}{}_{a_i a_j}$, for each unique atom pair [Li-Li, Li-Fe(II), and Fe(II)-Fe(II)] and distances between them, r_{ij}. The cutoff for the two-body terms

TABLE I. Crystallographic data of bulk $FePO_4$ and $LiFePO_4$ and corresponding computed data for structures in a ferromagnetic ordering.

Material	Space group	Materials project ID	Calc. a, b, c (Å)	Expt. a, b, c (Å)	Expt. Ref.
Fe(III)PO_4	*Pnma*	mp-20361	4.864, 5.899, 9.944	4.756, 5.752, 9.760	[39]
LiFe(II)PO_4	*Pnma*	mp-19017	4.736, 6.055, 10.418	4.695, 6.011, 10.338	[39]

was chosen to be 3.5 Å for Li-Li, 4.2 Å for Fe(II)-Fe(II), and 4.0 Å for Li/Fe(II) leading to 1, 1, and 3 constants, respectively. Long-range interactions are treated using an effective point charge model and Ewald summation as shown by the second term of the equation.

The charges of the Li and Fe(II) ions, q_{Li} and $q_{\mathrm{Fe(II)}}$, are described by a single parameter, $Q_{\mathrm{eff}} = q_{\mathrm{Li}} = -q_{\mathrm{Fe(II)}}$. Finally, the constant term describes the energy associated with introducing a noninteracting Li-Fe(II) pair to the lattice as well as accounting for the background matrix of PO_4. This is necessary when fitting the model to a dataset with varying concentrations of Li and associated Fe(II). The interaction parameters and effective charge were optimized using the DFT data in the software package CCS [37], then used as input for thermodynamic sampling in GULP [38]. Both the CCS and GULP codes are open source and freely available.

III. RESULTS AND DISCUSSION

In Sec. III A, we present results for the bulk systems and describe the structural models we use in the rest of the paper. In Sec. III B, we validate and test the OMC method for Fe(II) by calculations on a $[Fe(H_2O)_6]^{+2}$ octahedral complex and in a FP primitive cell. This section serves as a guide, providing insights into the practical application of the methodology and shedding light on the electronic properties of Fe(II) ions in various environments. In Sec. III C, we show the results from the Li and Va insertion and the formation of Li-Fe(II) and Va-Fe(III) pairs. In Sec. III D, we report on the results obtained from the thermodynamic sampling.

A. Structural and electronic properties of FP/LFP

There are many different crystal structures to choose from for FP and LFP as seen by the entries in the Materials project database [40]. The ground state of LFP is a unit cell of orthorhombic symmetry (space group *Pnma*), a configuration also presumed for the delithiated FP phase. For FP, this phase is thermodynamically slightly less stable than the computed ground state tetragonal structure, E_f, within 0.02 eV/atom above the hull [40], but has been observed experimentally [39]. The crystallographic data for the bulk phases investigated in the present paper are given in Table I and the unit cells for both the FP and LFP phases are shown in Fig. 1.

Both the FP and LFP phases exhibit antiferromagnetic ordering at low temperatures, transitioning to a paramagnetic state at 50 and 125 K, respectively [39,41]. Prior studies have indicated that the magnetic ordering in LFP and FP has a minor impact on the formation energies and the relaxation of the crystal structure [42]. This aligns with the findings presented in Table II. Therefore, for the sake of simplicity, all structures in the training set are treated in a ferromagnetic manner.

As a reference, the projected density of states (pDOS) of FP and LFP in the ferromagnetic states are shown in Figs. 2(a) and 2(b), respectively. In the figures, both spin channels are shown. Figure 2(b) shows additional occupied spin-down d states in LFP due to the Fe(II) formation. The computed band gaps are given in Table II, where we also report band gaps obtained for the other magnetic orderings. The value for the band gap varies slightly more for FP, but both are close to the ones computed in Ref. [6]. This further validates the use of a ferromagnetic ordering in the electronic structure calculations.

B. Validating the OMC methodology for Fe^{2+} ions

In the case of d elements such as Fe in LFP, the orbital occupancy is specified by two 5×5 matrices, one for each spin channel. The five diagonal elements of these matrices represent the occupation of the five d orbitals, while off-diagonal elements signify deviation from these ideal states. Thus, the eigenvalues of the matrix give the weighted orbital occupation and the sum of the eigenvalues gives the number of electrons on the atoms, and thereby the oxidation state [43].

As a first case to test and demonstrate the OMC method for Fe(II), an isolated $[Fe(H_2O)_6]^{+2}$ octahedral complex is used. Fe(II) in the $[Fe(H_2O)_6]^{+2}$ will be in a high-spin configuration with four unpaired electrons and should display a crystal field splitting, Δ_{oct}, between two high-energy e_g states and three low-energy t_{2g} states.

OMC+DFT+U calculations following the two-step procedure described in Sec. II A, however with only ionic relaxation, were applied on the $[Fe(H_2O)_6]^{+2}$ octahedra. To obtain an Fe(II) ion, two electrons were removed from the neutral complex, resulting in a Fe($3d^6$) electronic configuration. To compensate for the charged unit cell, a neutralizing negative background charge (jellium model) was applied. The

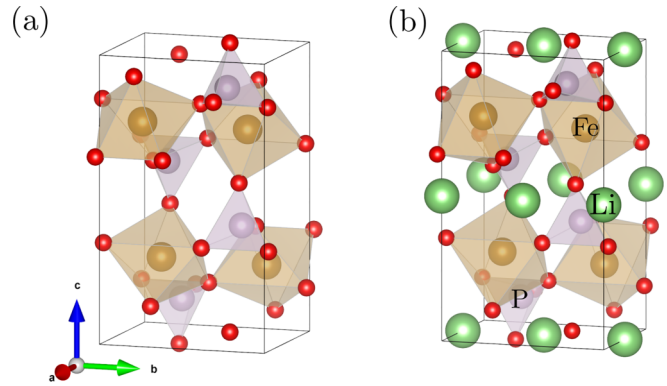

FIG. 1. The crystal structure of (a) $FePO_4$ and (b) $LiFePO_4$ with labels showing the respective chemical species: lithium (green), iron (brown), phosphorous (purple), and oxygen (red).

TABLE II. Computed lattice constants, formation energies, and band gaps for FP and LFP in a 2×2×2 supercell of different magnetic ordering.

	Ordering	a, b, c (Å)	V (Å^3)	ΔE_f (eV/atom)	E_g (eV)
$FePO_4$	Ferromagnetic	4.864, 5.899, 9.944	285.296	0.002	1.76
	Antiferromagnetic	4.858, 5.888, 9.942	284.367	0.000	2.20
	Paramagnetic	4.862, 5.892, 9.943	284.803	0.001	1.96
$LiFePO_4$	Ferromagnetic	4.736, 6.055, 10.418	298.726	0.010	3.40
	Antiferromagnetic	4.734, 6.052, 10.414	298.364	0.000	3.40
	Paramagnetic	4.736, 6.054, 10.412	298.490	0.002	3.39

electron occupation of both spin channels was controlled by the occupation matrix, with five electrons in the spin-up channel and one electron in the spin-down channel. This was done by specifying integer values (0 or 1) along the diagonal of the two 5×5 matrices, while the off-diagonal values were set to zero. These so-called diagonal occupation matrices have previously been used by Dorado *et al.* [44] and Miskowiec [45] for describing electron localization of 5f electrons in uranium. For the 5×5 matrix, this gives five different possibilities with different orbital occupation in the spin-down channel.

The resulting spin densities and corresponding total energy differences, ΔE, from the five OMC+DFT+U calculations for the $[Fe(H_2O)_6]^{+2}$ complex are shown in Figs. 3(a)–3(e). We note that the main effect captured in the energy difference, ΔE, originates from the occupation of different eigenstates. This implies that ΔE is a measure of Δ_{oct} described above. We estimate Δ_{oct} for the d orbitals in Fe(II) in the $[Fe(H_2O)_6]^{+2}$ complex d orbitals to be 0.64 eV. This is within the 0.46–0.83 eV range predicted in Ref. [46].

To investigate if a standard DFT+U calculation will find the low-energy state also without OMC control, we have generated 50 structures of the $[Fe(H_2O)_6]^{+2}$ complex, each initialized with a slight distortion where the positions of the atoms in the initial structure were displaced in a random direction following a normal distribution with a standard deviation of 0.1 Å and initializing the atomic density using randomized wave functions. After the geometry optimizations, we find that standard DFT+U captures the low-energy state in all 50 cases, i.e., the ΔE is similar as that of the ones found for the low-energy t_{2g} using the OMC method. The spin density for a typical case shown in Fig. 3(f) resembles that of the low-energy t_{2g} spin density obtained with OMC+DFT+U [see Fig. 3(d)].

It is interesting to note that the spin density corresponding to the three degenerated low-energy t_{2g} and two high-energy e_g orbitals shown in Figs. 3(a)–3(e) resembles the atomic d orbitals expected from crystal field theory. We identify the

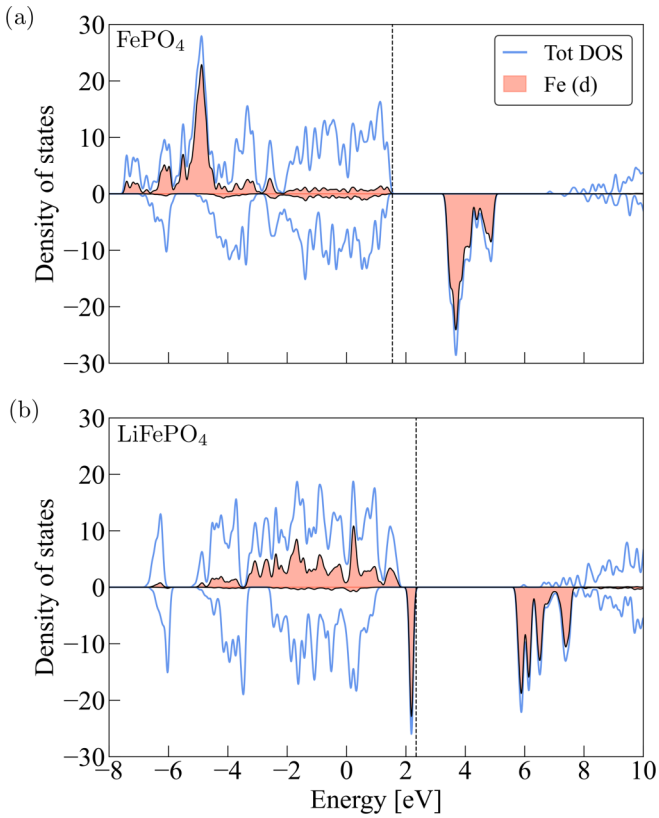

FIG. 2. Projected density of states (pDOS) for (a) $FePO_4$ and (b) $LiFePO_4$. Energies have been shifted by the alignment of the oxygen 2s orbitals. The dashed vertical lines show the Fermi level at the highest occupied electronic state.

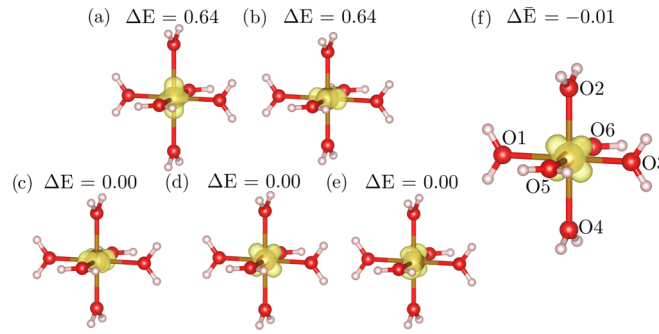

FIG. 3. Spin densities and total energy differences, ΔE, from OMC+DFT+U calculations for $[Fe(H_2O)_6]^{+2}$ corresponding to (a), (b) high-energy e_g states and (c)–(e) low-energy t_{2g} states. It is interesting to note that the spin densities resemble the corresponding d-atomic orbitals expected from crystal field theory: (a) $3d_{z_2}$, (b) $3d_{x^2-y^2}$, (c) $3d_{xy}$ (d) $3d_{yz}$, and (e) $3d_{xz}$. (f) Resulting spin density and total energy difference from DFT+U calculations without OMC. The spin density is shown for one structure, however the total energy difference is the average, $\Delta\bar{E}$, obtained from 50 different DFT+U calculations (see text for description). The isosurface level is plotted at 0.025 e/Å.

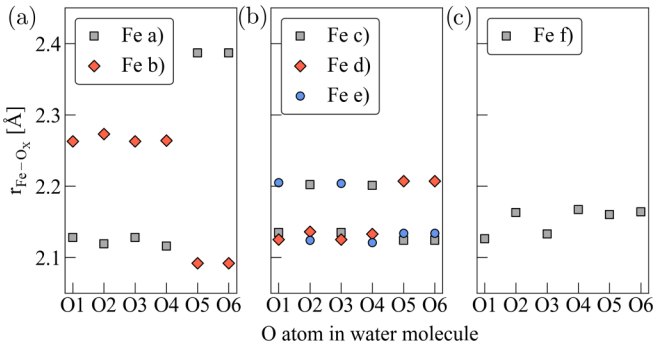

FIG. 4. Fe(II)-O_X bond lengths in $[Fe(H_2O)_6]^{+2}$ for the different cases presented in Fig. 3 [$x = 1 - 6$ as illustrated in Fig. 3(f)]. Bond lengths for the structures with occupied (a) high-energy e_g states, (b) low-energy t_{2g}, and (c) the representative DFT+U structure given in Fig. 3(f).

typical t_{2g} orbital orientation with lobes pointing out into the empty space and the typical e_g orientation with lobes pointing directly toward the ligands. These observations are also confirmed by larger bond lengths along these directions when occupying e_g states with the extra spin-down electron (see Fig. 4). In Fig. 4(a), the Jahn-Teller distortion obtained for the high-energy e_g state is presented. Figure 4(b) shows smaller distortions obtained for the low-energy t_{2g} state. Figure 4(c) demonstrates the lack of distortion obtained without OMC which leads to the fractional occupation of all d orbitals. This highlights the importance of going beyond standard DFT+U calculations when studying effects related to structural distortions originating from specific orbital occupations.

Fe is also sixfold coordinated in bulk FP, but with five closest neighbors and one in the next nearest shell (see Fig. 5). The primitive structure thereby lacks the perfect octahedral symmetry we have in the $[Fe(H_2O)_6]^{+2}$ complex investigated above, and is therefore expected to have a smaller energy splitting. We have followed the same procedure as above for Fe(II) in FP by adding one electron to the FP unit cell, again compensated by a neutralizing positive background charge. This additional electron placed on one Fe iron changes the Fe-O bond distances and is localized as the structure distorts in order to adjust to its presence. This leads to the formation of a localized polaronic state, Fe(II). These states appear in the

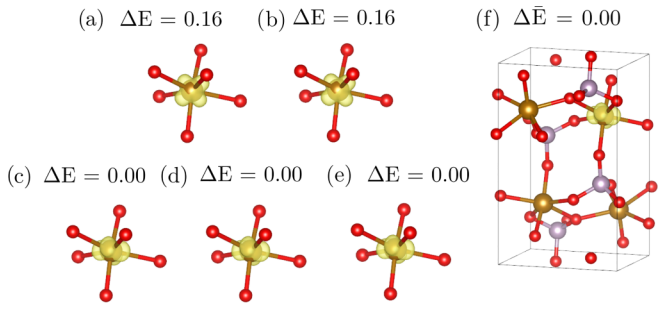

FIG. 5. Spin density plots of $[FePO_4]^{-1}$ with energies in eV showing (a)–(e) five different cases of attempted orbital configurations using OMC+DFT+U and (f) average energy for 50 DFT+U calculations without OMC. The configurations are ordered by their energy and the isosurface level is plotted at 0.025 e/Å.

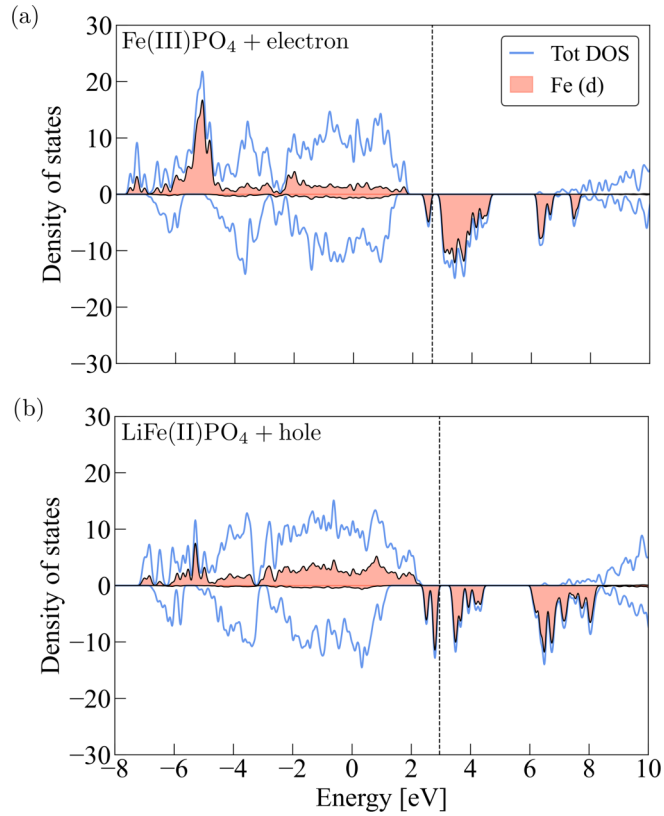

FIG. 6. Projected density of states (pDOS) of (a) FP with an additional electron as illustrated in Fig. 5(d) and (b) a LFP with a hole, produced in the same way. Energies have been shifted by the alignment of the oxygen 2s orbitals. The dashed vertical lines show the Fermi level at the highest occupied electronic state.

band gap in the density of states for the spin-down channel [see Fig. 6(a)].

The spin densities obtained from the OMC+DFT+U calculations for FP are not as clearly interpreted as they were for the octahedral Fe(II) complex discussed above. Still, there is a clear division into two states at higher energy and three levels at lower energy. The high-energy states [Figs. 5(a) and 5(b)] are found to lie in the ba plane and close to the $3d_{xy}$ state in Fig. 3(c). The low-energy states [Figs. 5(c)–5(e)] are seemingly like the $3d_{yz}$ state in Fig. 3(d). Compared to the hydrated Fe(II) ion, the total energy difference between occupation of low- and high-energy states is smaller in the solid, $\Delta E = 0.16$ eV.

Again, as a comparison we performed relaxations without OMC for 50 slightly distorted structures (using the same procedure as for the $[Fe(H_2O)_6]^{+2}$ complexes but with 0.05 Å in standard deviation). The average energy from the 50 unconstrained DFT+U calculations [Fig. 5(f)] reaches the same value as the low-energy OMC structures. These studies confirm that the OMC procedure does not affect the ground state energy but gives additional control on polaron localization and occupation in the structure.

A similar procedure has been applied to an LFP primitive cell, were one electron is removed in order to generate a hole polaron [Fe(III)]. The electronic structure showing Fe(III) is presented in Fig. 6(b). Similarly, both the

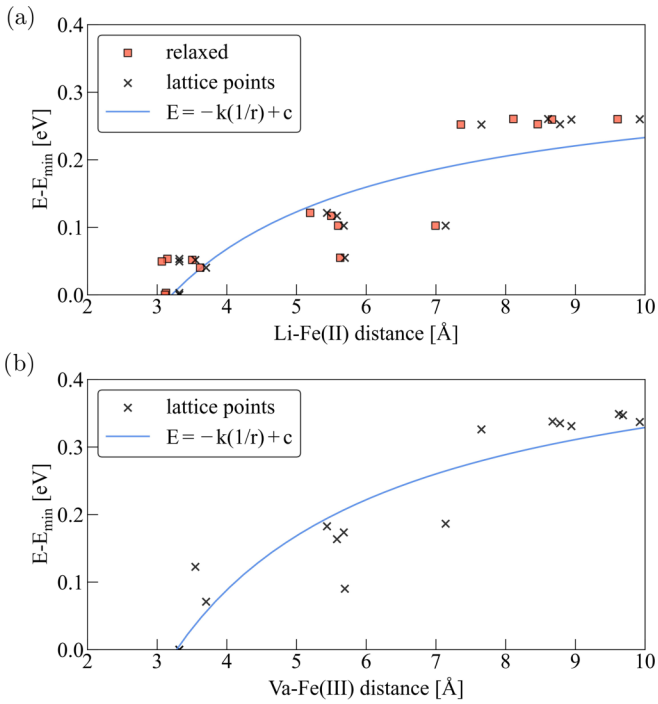

FIG. 7. Energy vs distance for (a) Li-Fe(II) and (b) Va-Fe(III) where Li/Va has been placed in 16 symmetry nonequivalent positions. A Coulomb potential (E) with (a) $k = 1.10, c = 0.34$ and (b) $k = 1.60, c = 0.49$ is fitted on the LFP lattice points for each case and included as a guide. Note that the fitting in this case does not consider the periodicity of the supercell.

unconstrained DFT+U and the OMC+DFT+U procedures find the ground state with energy differences down to the fourth digit.

C. Polarons in $FePO_4$/$LiFePO_4$

In this section the OMC+DFT+U method is used to investigate the interaction between intercalated Li/Va and their associated Fe(II)/Fe(III) in the dilute limits. We use a 2×2×2 supercell with one or two Li-Fe(II)/Va-Fe(III) pairs corresponding to a concentration of 3.125 and 6.25%, respectively. Multiple configurations with different separations between the Li and Fe(II) were considered. In the previous subsection we found that the $3d_{xz}$ orbital configuration had the lowest energy for a single electron polaron in the FP lattice. The same occupations was enforced, using the OMC method, on all Fe(II) ions in the calculations presented here. A ferromagnetic ordering of the spins is imposed in all cases.

First, we computed 16 configurations for a single Li-Fe(II)/Va-Fe(III) pair at 16 symmetry nonequivalent separations, spanning up to 10 Å in an FP cell. We confirmed that the localization of the polaron on the chosen Fe site was successful by inspecting the magnetic moments of all Fe ions in the structures. Figure 7(a) shows a scatter plot of the relative energies (setting the lowest-energy configuration at zero) for all these configurations as a function of the distance between the Li ion and Fe(II).

The first coordination sphere is under 4 Å with five possible closest neighbors and the second sphere is between 5 and 7.2 Å. Results for the Va-Fe(III) case are similarly presented in Fig. 7(b), with the vacancy lattice points corresponding to Li lattice positions. We note that the relaxation effect of the Li-Fe(II) separation is small by comparing the optimized distances with the lattice points of the cell. Calculating the optimized distance between Va-Fe(III) has been opted out, due to the added complication of finding the center of mass of the vacant site.

Despite using the OMC procedure, it is still difficult to trap the polarons in the high-energy structures. When turning off the OMC control, two of the high-energy Li-Fe(II) structures changed site location. This change should not significantly impact our results, as we still possess a diverse set of structures with varying energies. We note that our reported values closely match those given in Ref. [21] up to 7 Å. In the Li-Fe(II) case, energies are in accordance with Ref. [15] within the same range.

Overall, both interactions seem to follow a Coulomb-like behavior as can also be inferred from the fitted $1/r$ curves shown in Fig. 7. In Fig. 7(a), the fitted line corresponds to an effective charge for the Li ion of 0.3 e, or equivalent to a static dielectric constant of 13.1 assuming a charge of +1 for the Li ions. In Fig. 7(b) for one Va-Fe(III) pair in LFP, the equivalent value is 9.0. In comparison, Ref. [47] report a value of 11.6 for LFP which was motivated by other inorganic phosphates having a dielectric constant within the range of 4.6–10.7 [48]. Reference [49] used the same procedure as Ref. [47] but included structures over the whole concentration range and reported a value of 17.5 for FP and 19.8 for LFP. This would indicate a higher screening in LFP which is not reflected in our results.

This discrepancy is further investigated by DFT+U calculations on bulk FP and LFP structures using perturbation theory [50]. For the case of bulk FP, the total dielectric constant including both electronic and ionic contributions is an isotropic tensor with values of (9.1,18.0,10.2). The corresponding value for LFP is (9.0,9.6,8.4), which is on average lower than for FP which further proves the consistency of our data.

Next, we consider two Li-Fe(II)/Va-Fe(III) pairs in the same supercell. These calculations allow us to also investigate Li-Li/Va-Va and Fe(II)-Fe(II)/Fe(III)-Fe(III) interactions. The *ac* plane of LFP can be seen in Fig. 8(a) with Li-Li distances of 4.7 and 5.7 Å. However, a second Li can also be placed in the next *ac* plane, either at 3.0 or 6.5 Å as seen in Fig. 8(b). A total of 29 structures were generated with Fe(II) and Fe(III) at various positions and Li/Va at a maximum distance of 6.5 Å.

The results for the structures containing two pairs are presented in Fig. 9 showing the variation in energy depending on the Li-Li and Va-Va distance and the distance to and between their respective polarons. Figures 9(a) and 9(c) show the distribution of the average distance while Figs. 9(b) and 9(d) show the distribution of the Fe(II)-Fe(II) and Fe(III)-Fe(III) distances.

We see a large spread in energies for the different configurations within each group, up to 0.6 eV. Structures with shorter Li-Li distances have overall higher energy indicating possible repulsive forces between these species. In Fig. 9(a), we see that shorter average distances between Li and Fe(II) give lower energies. For the Va case, the low-energy structure with

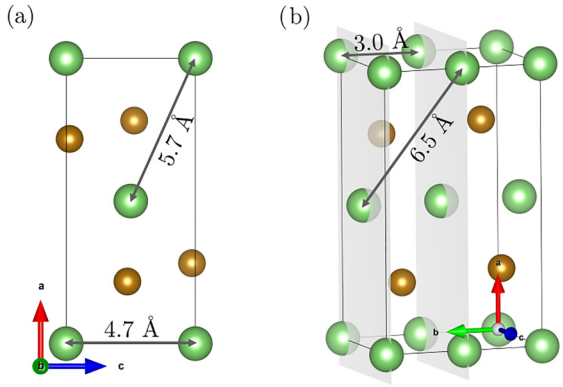

FIG. 8. The crystal structure of $LiFePO_4$ showing (a) the *ac* plane and (b) a three dimensional rendering of multiple such *ac* planes separated at 3.0 Å. Here, lithium is in green and iron is in brown. Oxygen and phosphorus have been excluded for visualization purposes.

4.7 Å Va-Va separation is notably more stable. The picture is more complete when combined with Figs. 9(b) and 9(d), where the change in distance between the polarons seems to have a more prominent effect.

The absence of a correlation between energies and polaron distances suggests that additional factors, beyond these parameters, are influencing the system. One such factor is the shielding of polarons from each other by Li. It is noteworthy that this shielding effect manifests differently in the case of Va. The designation of Va as a species is primarily for modeling purposes, when it in its actuality represents a vacant

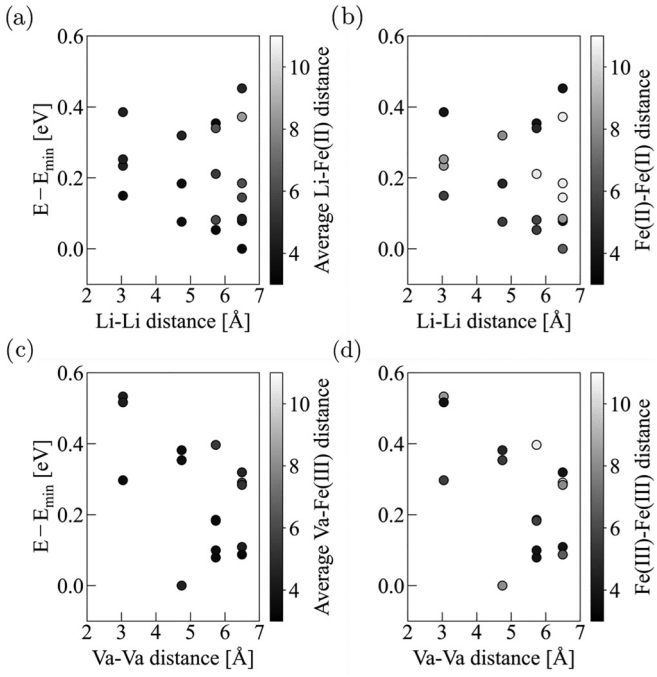

FIG. 9. OMC+DFT+U calculated energies of two pairs of either Li-Fe(II) or Va-Fe(III) in a 2×2×2 cell showing the scattering in energy with (a) average Li-Fe(II) distance, (b) Fe(II)-Fe(II) distance, (c) average Va-Fe(II) distance, as well as (d) Fe(III)-Fe(III) distance. All distances are given in Å.

TABLE III. Fitted parameters in the interaction model described in Sec. III C [see Eq. (1)].

r_{cut} (Å)	a_i	a_j	C (eV)
$Q_{eff} = q_{Li} = -q_{Fe(II)} = 0.26e$			
3.5	Li	Li	0.01
4.2	Fe(II)	Fe(II)	0.19
4.0	Li	Fe(II)	−0.01
4.0	Li	Fe(II)	0.04
4.0	Li	Fe(II)	0.00
$Q_{eff} = -q_{Va} = q_{Fe(III)} = 0.33e$			
3.5	Va	Va	0.13
4.2	Fe(III)	Fe(III)	−0.05
4.0	Va	Fe(III)	−0.02
4.0	Va	Fe(III)	0.07
4.0	Va	Fe(III)	0.03

Li site within the lattice. These results emphasize the intricate nature of this system, where structural stability is evidently sensitive to the specific arrangement of polarons.

D. Temperature dependence

As discussed in the Introduction, a temperature dependence in the correlation between the polaronic and Li-Va sublattices has been reported [24]. To investigate and quantify this dependence in Li-Li/Va-Va, Li-Fe(II)/Va-Fe(III), and Fe(II)-Fe(II)/Fe(III)-Fe(III) arrangements, we have fitted interaction models to the DFT+U data from Sec. III C and performed a series of Monte Carlo simulations. To account for the dissimilar electrostatic conditions in FP and LFP, as presented by the DFT+U results (Sec. III C), two different interaction models have been generated.

1. Fitting an interaction model

The interaction model used in the Monte Carlo simulations was described in Sec. II B and is defined by two parameters, the two-body interaction terms C and the effective charge, Q_{eff}. These parameters are fitted to the OMC+DFT+U data for the 16+29 configurations containing one and two Li and their associated Fe(II); see Sec. III C for details. We include all structures in the numerical fit of the model, both the ones containing one and two Li. The Va-Fe(III) data were fitted analogously. The mean squared error of the fit for the Li-Fe(II) structures is 2.3 meV and for Va-Fe(III) it is 1.6 meV. Table III give the values for all the fitted parameters of the models. We obtain an effective charge, Q_{eff}, of $0.26e$ and $0.34e$ for the Li and Va case, respectively. The larger value of the Va-Va interaction parameter compared to Li-Li indicates a higher repulsive force. We note the similarity of the effective charge fitted here using a full Ewald treatment and the one obtained from the simple line fit to a Coulomb potential in Sec. III C.

2. Statistical sampling

A series of Monte Carlo simulations were performed between 100 and 1000 K which is the region of interest in the phase diagram of LFP [2,3]. A (4×8×8) supercell is used

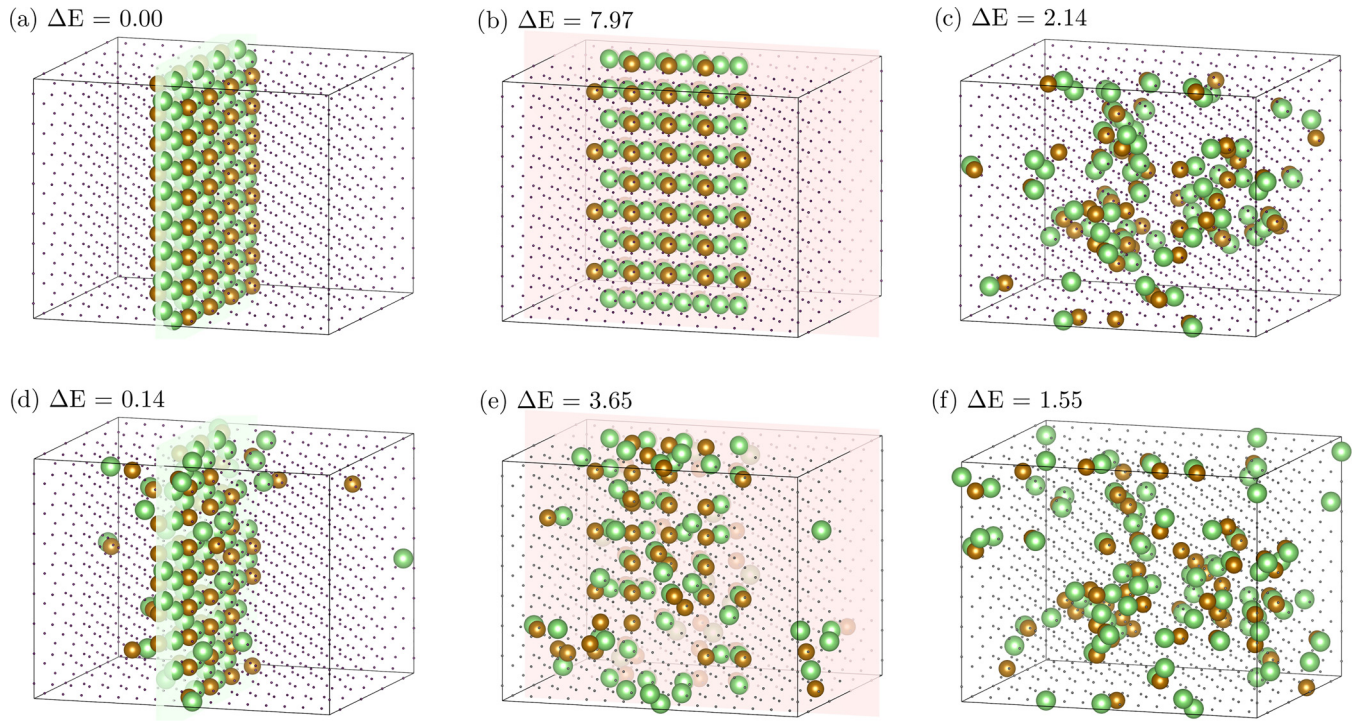

FIG. 10. Initial structures for Li-Fe(II) (a) with a constructed ordered initial arrangement in the *ac* plane, (b) with a constructed ordered initial arrangement in the *bc* plane, and (c) after an MC equilibration simulation. Snapshots of the resulting Monte Carlo trajectories at 300 K are depicted in (d), (e), and (f), respectively. The $T = 0$ K energy difference in eV is predicted using the generated interaction model. Li is represented in green, Fe(II) in brown, and Li vacancies as black dots. O, P, and Fe(III) are omitted for clarity. The *ac* and *bc* planes are illustrated for reference.

consisting of 2048 lattice sites. We use a number of Li and Va corresponding to an overall stoichiometry of $Li_{0.0625}FePO_4$ and $Li_{0.9375}FePO_4$ and perform MC simulations for these separate cases. This corresponds to the same concentrations as our DFT+U data consisting of two Li in a 2×2×2 supercell. As a reference, we have included results from an MC simulation with an identical simulation cell but with no interaction between the species, a so-called hard-sphere model.

Previous theoretical and experimental results indicate a preference for the Li atoms to position into planar arrangements in the *ac* plane [51,52]. To investigate the stability of such planes using our model, we have considered three different cases of atomic arrangements as seen in Fig. 10. The first one is a supercell with atoms in the *ac* plane shown in Fig. 10(a), the second is similarly arranged but in the *bc* plane as shown in Fig. 10(b), and the third case is a structure obtained from an equilibration run of 2 000 000 trial moves as shown in Fig. 10(c). These are used as inputs in separate MC simulations where each trial move consists of a random swap of either a Li-Va or a Fe(II)-Fe(III). For the *ac* and *bc* plane, statistics were collected over 200 000 trial moves. For the already equilibrated simulation, statistics were collected over 20 000 trial moves.

Snapshots from the resulting trajectories are shown in Figs. 10(d)–10(f). The 0 K energies of the structures are calculated using the fitted interaction model for both the initial and resulting snapshots. In agreement with the theoretical study in Ref. [51], Fig. 10(a) shows the lowest-energy configuration of Li-Fe(II) to be in the *ac* plane. The agreement between the 0-K results and those in Ref. [51] is expected, given the absence of temperature effects. During the Monte Carlo simulations, temperature is seen to have a significant impact on the short-range ordering in the structures. Consequently, both the *ac* and *bc* planar structures gradually disintegrate, eventually converging to a similar state to that depicted in Fig. 10(f). Similar results have been obtained for the Va-Fe(III) system.

To determine whether or not these simulations have reached an equilibrated state, it is important to evaluate their sampling efficiency. This assessment has been carried out by computing the acceptance ratio for some indicative cases (see

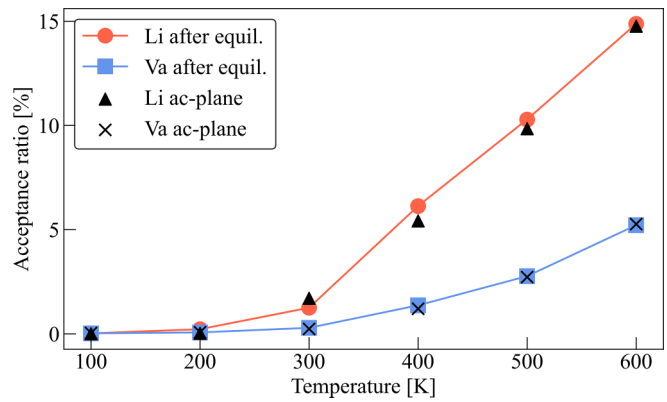

FIG. 11. Acceptance ratio, i.e., percentage of accepted attempts during the Monte Carlo simulations, at varying temperature initiated either after an equilibration run or with an ordered atomic arrangement in the *ac* plane.

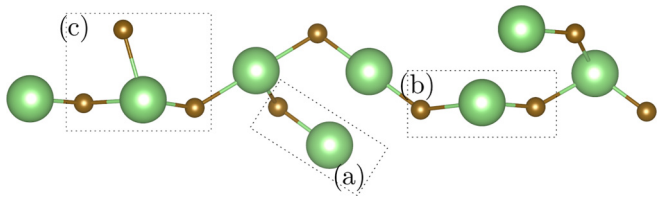

FIG. 12. A typical linked cluster from the Monte Carlo simulation showing examples of different coordination types: (a) 1 Fe(II)/Li, (b) 2 Fe(II)/Li, and (c) 3 Fe(II)/Li.

Fig. 11). A low acceptance ratio, as can be seen for temperatures between 100 and 300 K, indicates a trapped metastable state. The thermal energy at those temperatures might not be sufficient to transition the system into states of lower energy. In addition, we see a shift in the acceptance ratio for the Va case. This is due to the stronger Va-Fe(III) interaction as seen in Figs. 7(b) and 9. A trial move that separates the Va and Fe(III) pair has a higher probability of being rejected. As all three simulations reach a similar state, we conclude that the used algorithm leads to well-equilibrated structures within a finite number of MC steps at $T = 300$ K and above.

The equilibrated structures are seemingly disordered, but actually exhibit short-range ordering. This ordering can be quantified by examining their coordination. The Li-Fe(II) coordination sphere is defined with a cutoff radius of 4 Å, which includes the five closest neighbors as seen in the energy plot presented in Fig. 7(a). The Li-Li distances are presented in the structure in Fig. 8 and the coordination cutoff is set as 7 Å.

Figure 12 displays a representative chain cluster with different Li-Fe(II) coordination according to the chosen cutoff values. A zero-coordinated species [0 Fe(II)/Li] is isolated, a one-coordinated species [1 Fe(II)/Li] is in the form of a dimer, while higher coordination indicates clustering of some sort. The cluster can be in the form of a chain, one-coordinated end members linked by two-coordinated pairs, or three-dimensional clustering coordinated with three or more species.

Further analysis has been conducted on all MC calculations at temperatures 200–1000 K. These calculations were generated using the same procedure as in Fig. 10(f), starting from an initial equilibration. The 100-K data have been omitted due to the low acceptance ratio. The results from the MC simulations are presented in Fig. 13, which shows the coordination and average cluster size of Li-Fe(II) and Va-Fe(III) as a function of temperature. As expected, the average coordination of Li-Fe(II) and Va-Fe(III) decreases with increasing temperature. For the case of Li-Fe(II) in Fig. 13(a), we note a rather sharp increase in the amount of Li that coordinates only one Fe(II) at around 200 K, reaching 0.6 and decreasing slightly until reaching an almost constant value of about 0.5. In contrast, we see a gradual, albeit steady, increase in the amount of uncoordinated Li ions, starting to rise from a value close to zero at 200 K and reaching a value of about 0.4 at 1000 K.

The coordination is different in the Va case [see Fig. 13(d)], where it is initially higher and consists of more twofold and threefold coordinated pairs. This observation aligns with the higher binding energies reported in Ref. [16] as well as the results we see in Fig. 7(b) where larger Va-Fe(III) separations are higher in energy as compared to Li-Fe(II). Another discrepancy is found for the one-coordinated pairs, which increase from 0.1 to 0.6 within a larger temperature range. Similarly to the Li-Fe(II) case in Fig. 13(a), the fraction of

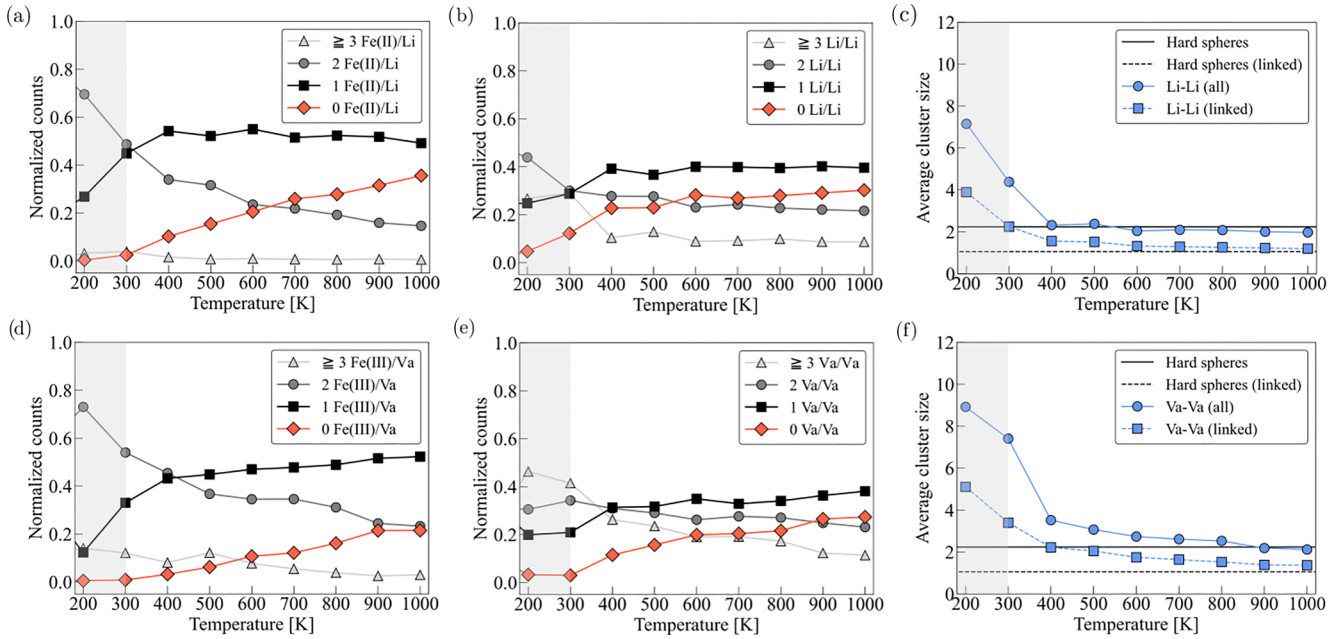

FIG. 13. Coordination plots from the Monte Carlo simulations of 4×8×8 supercells at 6.25 or 93.75% lithiation with (a) coordination between every Li-Fe(II) at 4 Å cutoff distance and (b) Li-Li at 7.0 Å cutoff, (c) average cluster size for Li-Li, (d) coordination of Va-Fe(III) at 4 Å cutoff distance, (e) Va-Va at 7.0 Å cutoff distance, and (f) average cluster size for Va-Va. The clusters are either (i) all Li/Va within 7 Å or (ii) all Li/Va linked by a Fe(II)/Fe(III). The reference hard-sphere model has been modified with a Li/Va cutoff distance of 4 Å. The shaded region indicates an acceptance ratio of $\leqslant$1.25%.

uncoordinated Va increase in a steady manner with temperature, however only reaching at most 0.2.

To summarize, the change in coordination of Li-Fe(II) and Va-Fe(III) in Figs. 13(a) and 13(d), respectively, is present across all temperatures. However, the transition to isolated and single pairs is shifted in temperature for the latter case. That we have an increase up to 40% isolated Li challenges the conjecture that Li-Fe(II) are being associated into pairs as postulated by Ellis *et al.* [12]. A study by Cabana *et al.* [24] on metastable solid solutions indicates a decoupling between these two sublattices with increased temperature. Our results are in agreement with the latter observation while also quantifying the percentage of uncoupled Li-Fe(II).

To further explore the system, we investigate the Li-Li and Va-Va pairing. There are very few Li-Li/Va-Va pairs within 4 Å; at most 11 and 16% of the Li and Va are found in such situations, respectively. It is interesting to note the difference between the amount of such pairs to what could have been in a completely disordered system. In the reference hard-sphere model, the corresponding value is 12%. To create a system with similar characteristics, we modify the reference hard-sphere model by imposing a restriction: the Li/Va species are not allowed to approach each other within a distance of 4 Å.

Beyond 4 Å, Li-Li and Va-Va neighbors are frequently present in the next nearest shell which is revealed by coordination plots presented in Figs. 13(b) and 13(e). These figures show a high fraction of Li/Va coordinating one or two Li/Va neighbors. This indicates the presence of dimers (composed of only one-coordinated members) and chains (composed of one- and two-coordinated members); see such an example in Fig. 12.

Three-dimensional clusters are scarce as can be seen from the low occurrences of Li/Va coordinating more than two Li/Va neighbors. Inspecting snapshots from the MC simulations, we found that many of the Li/Va clusters seem to be connected with bridging Fe(II)/Fe(III) ions, like the one depicted in Fig. 12.

In an attempt to quantify this observation we have computed the average size of Li/Va clusters in which each member is linked to its neighbors via Fe(II)/Fe(III) ions located at a short distance (<4 Å) from the connected Li/Va members. Figures 13(c) and 13(f) show the average size of these "linked" clusters. Specifically, we consider two scenarios.

(i) We define a cluster as all Li atoms within a 7 Å radius.

(ii) We identify clusters as Li atoms beyond 4 Å that are linked by a polaron neighbor.

Here, we also show the values for the modified hard-sphere model analyzed in the same way. Note that the maximum size for a cluster is limited to the number of Li or Va in the simulation cell which is 64. With increasing temperature, the average size of the clusters decreases, approaching that of the modified hard-sphere reference. These findings are consistent with the number of isolated Li/Va observed in the MC simulations. This fraction is 32.8 and 24.3% for the Li case and Va case at 1000 K compared to 25.2% in the modified hard-sphere case.

Clearly, an appreciable amount of such clusters are present, over the entire temperature range, in both the Li and Va case, as compared to the hard-sphere case. The measured distances between the atoms in the clusters at 400 K are depicted in Fig. 14. The same distances have been illustrated in Fig. 10. This reveals that most Li-Li and Va-Va atoms maintain a distance of 6.5 Å. The low occurrence of these atoms within 4.7 Å indicates a lack of arrangement in the *ac* plane, as already seen from Fig. 10(f).

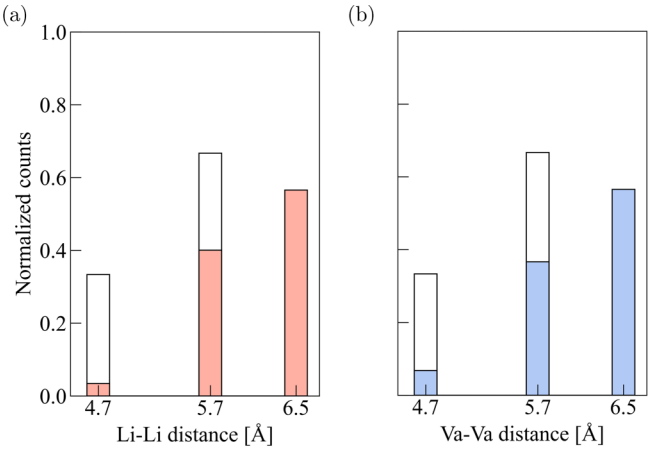

FIG. 14. Measured distances within clusters including two or more Li/Va at a temperature of 400 K for (a) Li-Li and (b) Va-Va. The uncoloured histogram corresponds to the perfect ordering of the *ac* plane in Fig. 10(a).

In short, our findings consistently indicate a more pronounced clustering behavior between Va-Fe(III) as compared to Li-Fe(II). The Va-Fe(III) is a model for the delithiation process during battery operation, where removal of Li atoms forms Va-Fe(III) pairs leading to the formation of $FePO_4$. Enhanced clustering in $FePO_4$ suggests a reduced energy barrier for phase initiation. This in turn implies a less stable solid solution. This is evidenced by the higher fraction of coordinated clusters, highlighting a less pronounced solid solution behavior. The shift in acceptance ratio with temperature (see Fig. 11) further corroborates this. These results indicate that it is more likely to form a solid solution near LFP, which is in accordance with findings by Phan *et al.* [18].

It should be emphasized that the DFT+U data and the MC simulations were performed at two extreme cases at the dilute limits. The boundaries of the phase diagram indicate a shift and asymmetry of the lithiation and delithiation process, with an eutectoid point at $x_{\mathrm{Li}} \approx 0.6$ [2,3]. The shown results of the different clustering behaviors of Li and Va suggest an explanation of the asymmetry of the phase diagram. However, more studies need to be conducted in order to fully comprehend the lattice dynamics and their effects at intermediate concentrations.

IV. CONCLUSION

We have investigated $\mathrm{Li}_x\mathrm{Va}_{1-x}\mathrm{Fe(II)}_x\mathrm{Fe(III)}_{1-x}\mathrm{PO}_4$ from first principles by explicit control of both Li and electronic degrees of freedoms. The presented method of using OMC+DFT+U results in a controlled localization of electron and hole polarons, allowing the placement of one and two Li-Fe(II) or Va-Fe(III) pairs at varying separations. The generated data are used to quantify interactions in terms of a Coulomb potential with a short-range correction considering only closest neighbors, motivated by the $1/r$ form of the

energy increase at larger separations. This interaction model is used to investigate the short-range charge ordering of multiple pairs using lattice-based Monte Carlo simulations.

In the Monte Carlo simulations (spanning up to 1000 K) we see virtually no association, neither of Li-Li nor of Va-Va at nearest neighbor distances. The generated trajectories display a solid-solution-like phase with a short-range ordering. We observe a strong indication of Li-Li and Va-Va association in the next nearest neighbor shell, separated by about 6.5 Å and bridged with Fe(II)/Fe(III), respectively. This results in a clear preference to form chains rather than three-dimensional clusters. With increasing temperature, these chains dissociate into smaller units as the system goes towards a complete random ordering.

Clustering of this sort is more present in the Va case, which is consistent with the OMC+DFT+U data and the larger effective charge of the Va in the fitted Coulomb model. This is mirrored in the computed fraction of isolated Li/Va that does not coordinate with any Fe(II)/Fe(III). With increasing temperature, these fractions gradually increase up to 40 and 20%, for Li and Va, respectively, challenging the simplified picture of a complete Li-Fe(II) pairing.

To conclude, the presented methodology allows for the quantification of Li-Li, Va-Va, Li-Fe(II), and Va-Fe(III) interactions in a controlled manner. Their interactions are mainly found to be governed by electrostatic forces, which is often overlooked in many models attempting to describe these systems. Despite a rather strong coupling at low temperatures, we note that already at normal battery operating conditions, a significant fraction of short-range charge ordering is present. This short-range ordering implies an enhanced $FePO_4$ phase formation during battery cycling and a higher solid solution stability during the delithiation process. In a broader picture, these results further emphasize the importance of using a two-sublattice description to accurately describe the intercalation thermodynamics of the LFP system.

ACKNOWLEDGMENTS

The project was funded by the European Union's Horizon 2020 Research and Innovation Program under Grant No. 957189 (BIG-MAP project), the Swedish Electromobility Center, the National Strategic e-Science program eSSENCE, and Stand Up For Energy. The computations were performed at NSC Tetralith provided by the National Academic Infrastructure for Supercomputing in Sweden, partially funded by the Swedish Research Council through Grant Agreement No. 2022-06725.

[1] A. Manthiram, A reflection on lithium-ion battery cathode chemistry, Nat. Commun. **11**, 1550 (2020).

[2] C. Delacourt, P. Poizot, J.-M. Tarascon, and C. Masquelier, The existence of a temperature-driven solid solution in Li_xFePO_4 for $0 \leqslant x \leqslant 1$, Nat. Mater. **4**, 254 (2005).

[3] J. L. Dodd, R. Yazami, and B. Fultz, Phase diagram of Li_xFePO_4, Electrochem. Solid-State Lett. **9**, A151 (2006).

[4] A. Yamada, H. Koizumi, N. Sonoyama, and R. Kanno, Phase change in Li_xFePO_4, Electrochem. Solid-State Lett. **8**, A409 (2005).

[5] A. Yamada, H. Koizumi, S. I. Nishimura, N. Sonoyama, R. Kanno, M. Yonemura, T. Nakamura, and Y. O. Kobayashi, Room-temperature miscibility gap in Li_xFePO_4, Nat. Mater. **5**, 357 (2006).

[6] K. Zaghib, A. Mauger, J. B. Goodenough, F. Gendron, and C. M. Julien, Electronic, optical, and magnetic properties of $LiFePO_4$: Small magnetic polaron effects, Chem. Mater. **19**, 3740 (2007).

[7] H. Liu, F. C. Strobridge, O. J. Borkiewicz, K. M. Wiaderek, K. W. Chapman, P. J. Chupas, and C. P. Grey, Capturing metastable structures during high-rate cycling of $LiFePO_4$ nanoparticle electrodes, Science **344**, 1252817 (2014).

[8] B. M. May, Y. S. Yu, M. V. Holt, F. C. Strobridge, U. Boesenberg, C. P. Grey, and J. Cabana, Nanoscale detection of intermediate solid solutions in equilibrated Li_xFePO_4 microcrystals, Nano Lett. **17**, 7364 (2017).

[9] B. Koo, J. Chung, J. Kim, D. Fraggedakis, S. Seo, C. Nam, D. Lee, J. Han, S. Jo, H. Zhao, N. Nadkarni, J. Wang, N. Kim, M. Weigand, M. Z. Bazant, and J. Lim, Dynamic surface phases controlling asymmetry of high-rate lithiation and delithiation in phase-separating electrodes, Energy Environ. Sci. **16**, 3302 (2023).

[10] A. K. Padhi, K. S. Nanjundaswamy, and J. B. Goodenough, Phospho-olivines as positive-electrode materials for rechargeable lithium batteries, J. Electrochem. Soc. **144**, 1188 (1997).

[11] C. Delacourt, J. Rodríguez-Carvajal, B. Schmitt, J. M. Tarascon, and C. Masquelier, Crystal chemistry of the olivine-type Li_xFePO_4 system ($0 \leqslant x \leqslant 1$) between 25 and 370 °C, Solid State Sci. **7**, 1506 (2005).

[12] B. Ellis, L. K. Perry, D. H. Ryan, and L. F. Nazar, Small polaron hopping in Li_xFePO_4 solid solutions: Coupled lithium-ion and electron mobility, J. Am. Chem. Soc. **128**, 11416 (2006).

[13] F. Zhou, T. Maxisch, and G. Ceder, Configurational electronic entropy and the phase diagram of mixed-valence oxides: The case of Li_xFePO_4, Phys. Rev. Lett. **97**, 155704 (2006).

[14] F. Zhou, Models for transition metal oxides and for protein design, Ph.D. thesis, Massachusetts Institute of Technology, 2006.

[15] T. Maxisch, F. Zhou, and G. Ceder, *Ab initio* study of the migration of small polarons in olivine Li_xFePO_4 and their association with lithium ions and vacancies, Phys. Rev. B **73**, 104301 (2006).

[16] S. P. Ong, V. L. Chevrier, and G. Ceder, Comparison of small polaron migration and phase separation in olivine $LiMnPO_4$ and $LiFePO_4$ using hybrid density functional theory, Phys. Rev. B **83**, 075112 (2011).

[17] M. D. Johannes, K. Hoang, J. L. Allen, and K. Gaskell, Hole polaron formation and migration in olivine phosphate materials, Phys. Rev. B **85**, 115106 (2012).

[18] A. T. Phan, A. E. Gheribi, and P. Chartrand, Modelling of phase equilibria of $LiFePO_4$-$FePO_4$ olivine join for cathode material, Can. J. Chem. Eng. **97**, 2224 (2019).

[19] R. Malik, F. Zhou, and G. Ceder, Kinetics of non-equilibrium lithium incorporation in $LiFePO_4$, Nat. Mater. **10**, 587 (2011).

[20] R. Malik, A. Abdellahi, and G. Ceder, A critical review of the Li insertion mechanisms in $LiFePO_4$ electrodes, J. Electrochem. Soc. **160**, A3179 (2013).

[21] Y. Sun, X. Lu, R. Xiao, H. Li, and X. Huang, Kinetically controlled lithium-staging in delithiated $LiFePO_4$ driven by the Fe center mediated interlayer Li–Li interactions, Chem. Mater. **24**, 4693 (2012).

[22] L. Barroso-Luque, P. Zhong, J. H. Yang, F. Xie, T. Chen, B. Ouyang, and G. Ceder, Cluster expansions of multicomponent ionic materials: Formalism and methodology, Phys. Rev. B **106**, 144202 (2022).

[23] X. Wang, J. Huang, Y. Liu, and S. Chen, The decisive role of electrostatic interactions in transport mode and phase segregation of lithium ions in $LiFePO_4$, Chem. Sci. **14**, 13042 (2023).

[24] J. Cabana, J. Shirakawa, G. Chen, T. J. Richardson, and C. P. Grey, MAS NMR study of the metastable solid solutions found in the $LiFePO_4/FePO_4$ system, Chem. Mater. **22**, 1249 (2010).

[25] I. Timrov, F. Aquilante, M. Cococcioni, and N. Marzari, Accurate electronic properties and intercalation voltages of olivine-type Li-ion cathode materials from extended hubbard functionals, PRX Energy **1**, 033003 (2022).

[26] J. P. Allen and G. W. Watson, Occupation matrix control of d- and f-electron localisations using DFT+U, Phys. Chem. Chem. Phys. **16**, 21016 (2014).

[27] G. Kresse and J. Furthmüller, Efficient iterative schemes for *ab initio* total-energy calculations using a plane-wave basis set, Phys. Rev. B **54**, 11169 (1996).

[28] G. Kresse and J. Furthmüller, Efficiency of *ab-initio* total energy calculations for metals and semiconductors using a plane-wave basis set, Comput. Mater. Sci. **6**, 15 (1996).

[29] J. P. Perdew, K. Burke, and M. Ernzerhof, Generalized gradient approximation made simple, Phys. Rev. Lett. **77**, 3865 (1996).

[30] G. Kresse and D. Joubert, From ultrasoft pseudopotentials to the projector augmented-wave method, Phys. Rev. B **59**, 1758 (1999).

[31] P. E. Blöchl, Projector augmented-wave method, Phys. Rev. B **50**, 17953 (1994).

[32] S. L. Dudarev, G. A. Botton, S. Y. Savrasov, C. J. Humphreys, and A. P. Sutton, Electron-energy-loss spectra and the structural stability of nickel oxide: An LSDA+U study, Phys. Rev. B **57**, 1505 (1998).

[33] A. Jain, G. Hautier, S. P. Ong, C. J. Moore, C. C. Fischer, K. A. Persson, and G. Ceder, Formation enthalpies by mixing GGA and GGA + U calculations, Phys. Rev. B **84**, 045115 (2011).

[34] M. Kick, C. Scheurer, and H. Oberhofer, Polaron-assisted charge transport in Li-ion battery anode materials, ACS Appl. Energy Mater. **4**, 8583 (2021).

[35] M. D. Radin and A. Van Der Ven, Simulating charge, spin, and orbital ordering: Application to Jahn-Teller distortions in layered transition-metal oxides, Chem. Mater. **30**, 607 (2018).

[36] J. Kullgren, M. J. Wolf, P. D. Mitev, K. Hermansson, and W. J. Briels, DFT-based Monte Carlo simulations of impurity clustering at CeO_2(111), J. Phys. Chem. C **121**, 15127 (2017).

[37] A. K. Akshay, E. Wadbro, C. Köhler, P. Mitev, P. Broqvist, and J. Kullgren, CCS: A software framework to generate two-body potentials using curvature constrained splines, Comput. Phys. Commun. **258**, 107602 (2021).

[38] J. D. Gale and A. L. Rohl, The general utility lattice program (GULP), Mol. Simul. **29**, 291 (2003).

[39] G. Rousse, J. Rodriguez-Carvajal, S. Patoux, and C. Masquelier, Magnetic structures of the triphylite $LiFePO_4$ and of its delithiated form $FePO_4$, Chem. Mater. **15**, 4082 (2003).

[40] A. Jain, S. P. Ong, G. Hautier, W. Chen, W. D. Richards, S. Dacek, S. Cholia, D. Gunter, D. Skinner, G. Ceder, and K. A. Persson, Commentary: The materials project: A materials genome approach to accelerating materials innovation, APL Mater. **1**, 011002 (2013).

[41] R. P. Santoro and R. E. Newnham, Antiferromagnetism in $LiFePO_4$, Acta Cryst. **22**, 344 (1967).

[42] M. Cococcioni and N. Marzari, Energetics and cathode voltages of $LiMPO_4$ olivines (M=Fe, Mn) from extended Hubbard functionals, Phys. Rev. Mater. **3**, 033801 (2019).

[43] P. H. Sit, R. Car, M. H. Cohen, and A. Selloni, Simple, unambiguous theoretical approach to oxidation state determination via first-principles calculations, Inorg. Chem. **50**, 10259 (2011).

[44] B. Dorado, B. Amadon, M. Freyss, and M. Bertolus, DFT+U calculations of the ground state and metastable states of uranium dioxide, Phys. Rev. B **79**, 235125 (2009).

[45] A. Miskowiec, Metastable electronic states in uranium tetrafluoride, Phys. Chem. Chem. Phys. **20**, 10384 (2018).

[46] E. Miliordos and S. S. Xantheas, Ground and excited states of the $[Fe(H2O)_6]^{2+}$ and $[Fe(H2O)_6]^{3+}$ clusters: Insight into the electronic structure of the $[Fe(H2O)_6]^{2+}$-$[Fe(H2O)_6]^{3+}$ complex, J. Chem. Theory Comput. **11**, 1549 (2015).

[47] M. S. Islam, D. J. Driscoll, C. A. Fisher, and P. R. Slater, Atomic-scale investigation of defects, dopants, and lithium transport in the $LiFePO_4$ olivine-type battery material, Chem. Mater. **17**, 5085 (2005).

[48] R. D. Shannon, Dielectric polarizabilities of ions in oxides and fluorides, J. Appl. Phys. **73**, 348 (1993).

[49] C. Kuss, G. Liang, and S. B. Schougaard, Atomistic modeling of site exchange defects in lithium iron phosphate and iron phosphate, J. Mater. Chem. **22**, 24889 (2012).

[50] M. Gajdoš, K. Hummer, G. Kresse, J. Furthmüller, and F. Bechstedt, Linear optical properties in the projector-augmented wave methodology, Phys. Rev. B **73**, 045112 (2006).

[51] A. Abdellahi, O. Akyildiz, R. Malik, K. Thornton, and G. Ceder, The thermodynamic stability of intermediate solid solutions in $LiFePO_4$ nanoparticles, J. Mater. Chem. A **4**, 5436 (2016).

[52] L. Gu, C. Zhu, H. Li, Y. Yu, C. Li, S. Tsukimoto, J. Maier, and Y. Ikuhara, Direct observation of lithium staging in partially delithiated $LiFePO_4$ at atomic resolution, J. Am. Chem. Soc. **133**, 4661 (2011).